

PET Instrumentation and Reconstruction Algorithms in Whole-Body Applications*

Gabriele Tarantola, BE; Felicia Zito, MSc; and Paolo Gerundini, MD

Department of Nuclear Medicine, Ospedale Maggiore di Milano, Istituto di Ricovero e Cura a Carattere Scientifico, Milano, Italy

The aim of this work is the presentation and comparison of state-of-the-art dedicated PET systems actually available on the market, in terms of physical performance and technical features. Particular attention has been given to evaluate the whole-body performance by sensitivity, spatial resolution, dead time, noise equivalent counting rate (NECR), and scatter fraction. PET/CT systems were also included as new proposals to improve diagnostic accuracy of PET, allowing effective anatomic integration to functional data. An overview of actually implemented reconstruction algorithms is also reported to fully understand all of the factors that contribute to image quality.

Key Words: PET instrumentation; PET physical performance; whole-body imaging; reconstruction algorithms

J Nucl Med 2003; 44:756–769

The great interest shown toward PET instrumentation is mainly due to the fact that with this technique real functional and quantitative imaging of the organs of interest can be performed. During the last 20 y, great efforts have been made to improve the diagnostic accuracy of this imaging modality through the development of new data acquisition/processing systems and the introduction of new β^+ -emitting radiopharmaceuticals. The turning point in PET development is undoubtedly represented by the introduction and approval by the Food and Drug Administration of ^{18}F -FDG as an oncologic PET radiotracer.

Nowadays, there is increasingly wide PET application for clinical diagnosis, even in centers lacking a cyclotron, thanks to the distribution of ^{18}F -FDG produced in licensed sites that are located within a reasonable distance of the imaging center.

In this scenario, PET scanners with different performance characteristics have been developed, including the hybrid gamma cameras and partial or full-ring dedicated tomo-

graphs, working in 2-dimensional (2D) or 3-dimensional (3D) mode, to meet different requirements and variable clinical workloads. The development of new reconstruction algorithms and improvements in computer speed and storage memory have led to the possibility of collecting and processing coincidence data within very short times, effectively improving image quality and patient throughput.

Furthermore, the recent introduction of new scintillation crystals (lutetium oxyorthosilicate [LSO] and gadolinium orthosilicate [GSO]) and the creation of PET/CT systems can improve the scanner's technical performance and, at the same time, increase the clinical effectiveness of PET imaging (1–8).

DATA ACQUISITION

True and Random Events

The principle followed by the PET scanner in data acquisition is to accept two 511-keV events, simultaneously detected by 2 crystals. Actually, to account for the time of flight of the 2 annihilation photons, the scintillation time, and the processing electronics, events within a short coincidence time window are accepted. The system assigns to coincidence events a line of response (LOR), corresponding to a straight line joining the points where the photons were detected. However, as shown on Figure 1, unrelated annihilation photons within the coincidence time window will also be detected as random coincidence events, superimposing a low-frequency noise on true events. The randoms rate (R) is strictly related to the singles counting rate (S_1 and S_2) of each detector and to the coincidence time window width (τ_c) by the following relation (5–7,9):

$$R = 2 \cdot \tau_c \cdot S_1 \cdot S_2 \quad \text{Eq. 1}$$

Therefore, a quadratic increase in randoms will be observed by increasing the radioactivity in the field of view (FOV), whereas a decrease will result from reducing τ_c .

Efforts have been made to increment the net true counting rate without incrementing random coincidences, by implementing faster systems with narrower coincidence time windows. The typical 12-ns coincidence window is still in use for bismuth germanate (BGO)-based PET systems, whereas it reduces to 8 ns for GSO and NaI and 6 ns for LSO-based systems (factory data).

Received Jul. 3, 2002; revision accepted Oct. 31, 2002.

For correspondence or reprints contact: Paolo Gerundini, MD, Department of Nuclear Medicine, Ospedale Maggiore di Milano, Istituto di Ricovero e Cura a Carattere Scientifico, Via F. Sforza 35, 20122 Milano, Italy.

E-mail: segrmnuc@policlinco.mi.it

*NOTE: FOR CE CREDIT, YOU CAN ACCESS THIS ACTIVITY THROUGH THE SNM WEB SITE (http://www.snm.org/education/ce_online.html) THROUGH MAY 2004.

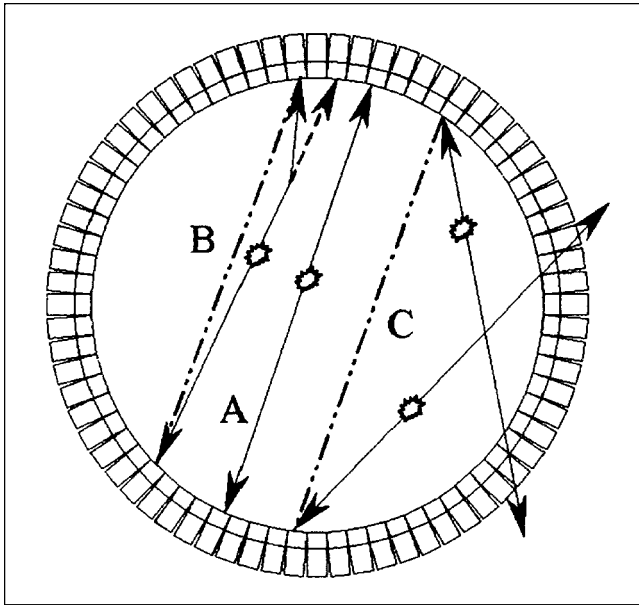


FIGURE 1. Graphic representation of true (A), scatter (B), and random events (C).

To correct for random events, a possible solution is to store all coincidence events or prompts (trues + scatter + randoms) and also all single events detected during data acquisition. Then the correction for randoms is performed by applying the above formula and subtracting the random events from prompts. This method is simple and efficient but requires a large memory and long processing times. A faster and more common way to perform this correction is by estimating randoms with the delayed coincidence window method. All coincidence events processed into the delayed window are known to be totally unrelated and consequently can be used for randoms estimation (5–7,9).

Scattered Events

Depending on photon energy and radioactivity distribution, a certain percentage of emitted events will interact in the body, being totally absorbed or deflected by a certain angle before detection. In the last case, Compton scatter occurs and the photon will lose energy proportionally to the angle between the original and the new trajectory (5–7,9).

Figure 1 shows, graphically, the difference between true, scattered, and random events.

The effectiveness of scatter removal is very important in nuclear medicine, because image blurring caused by scattered events may lead to important quantification errors. Ideally, the first and more practical way for scatter rejection should be the acquisition of only 511-keV events, requiring systems with very good energy resolution and a narrow-photoppeak energy window, thus excluding the majority of scattered photons. Actually, this cannot be achieved in practice, because PET scanners have limited energy resolution and a narrower energy window would also cause rejection of true events. On the basis of this consideration,

PET systems with lower energy resolution use wider energy windows and are affected by a larger scatter component (5–7,9). In fact, BGO-based scanners (energy resolution, about 25%) use a quite wide energy window (LLD = 300–350 keV and ULD = 650 keV) and have a larger scatter component than NaI(Tl)- or GSO-based scanners (energy resolution, 10%–15%; lower-level energy discriminator [LLD] = 435 keV and upper-level energy discriminator [ULD] = 590–665 keV) (factory data).

Traditionally used in PET scanners, an effective way to reduce scattered events is shielding by means of lead septa. In fact, in multiring PET scanners, septa interposed between detector rings significantly reduce the interplane scattered photons (5–9).

Mathematic compensation for scattered events is also possible and is necessary when there is a large scatter background that can degrade PET images. Some methods consist of simply estimating the scatter component by fitting or convolving the starting images with a priori defined deblurring filters (5,6,9). Others that are more rigorous and computationally intensive are based on Monte Carlo simulation and the Klein–Nishina formula (9).

System Dead Time

When a photon strikes a detector, the γ -ray is absorbed inside the crystal producing a light output, which is collected by several photomultiplier tubes (PMTs); the energy and spatial position of the event are then determined and finally the coincidence processing occurs.

The sum of the total time required to complete the above steps is defined as the system dead time (τ) and, during this time, the detection system is unable to collect new incoming γ -rays, which will be lost (5–7,9).

When working with high counting rates, count losses are mainly due to system dead time. A mathematic correction can be used to compensate for this effect by applying a multiplicative factor to measured counts. Obviously, when a too-high counting rate is reached, this approach ceases to be feasible.

Two possible solutions can be used to reduce system dead time: (a) creation of scanners with shorter crystal scintillation time and faster electronics (see all of the consideration concerning randoms counting rate); and (b) use of as-small-as-possible independent detection units by mean of small-sized PMTs and a lower number of dead PMTs for each detected event. This solution requires, however, a more complex and expensive detection system architecture.

EVALUATION OF PHYSICAL PERFORMANCE

Spatial Resolution

This parameter indicates the scanner's ability to distinguish 2 radioactive sources having a defined size and placed at a small relative distance. Its measurement is performed (10,11) by acquiring data from a low-activity radioactive point source in air (no scatter or random contribution) and measuring the full width at half maximum (FWHM, in mm)

of reconstructed count distribution (or point spread function [PSF]).

The final spatial resolution of the PET image results from various factors, some intrinsically related to the β^+ -annihilation interaction (noncollinearity of annihilation photons and positron range) and some related to the detection system, such as the scintillation crystal performance and electronics used (5–7,9).

One of the factors that produces the greatest degradation of this parameter is the limited intrinsic spatial resolution of the scintillation crystal. For the multicrystal PET scanner, the intrinsic spatial resolution is strictly related to the crystal size. This factor (c) is different depending on source radial position, being $d/2$ (d = crystal size) on the scanner axis and worsening toward the edge of the FOV. When small-sized crystals are grouped into blocks, a further loss due to errors in event localization must be considered (block effect).

The noncollinearity of annihilation photons is due to the physical state of the atoms interacting with positrons. In fact, the electron-positron mass center cannot be in a rest state; for this reason, the two 511-keV photons will be emitted with a smaller relative angle (at maximum, $\pm 0.25^\circ$) than 180° , determined by mass and energy conservation laws (Fig. 2). As a consequence, the detected LOR will not intersect the real annihilation point but will have a small variation around the correct direction. Fixing the distance D of the opposite detectors, the spreading C of the PSF can be evaluated as follows:

$$C = 0.0022 \cdot D. \quad \text{Eq. 2}$$

Therefore, this effect is much more evident as the detector ring diameter increases, which means a 1.5- to 2.0-mm

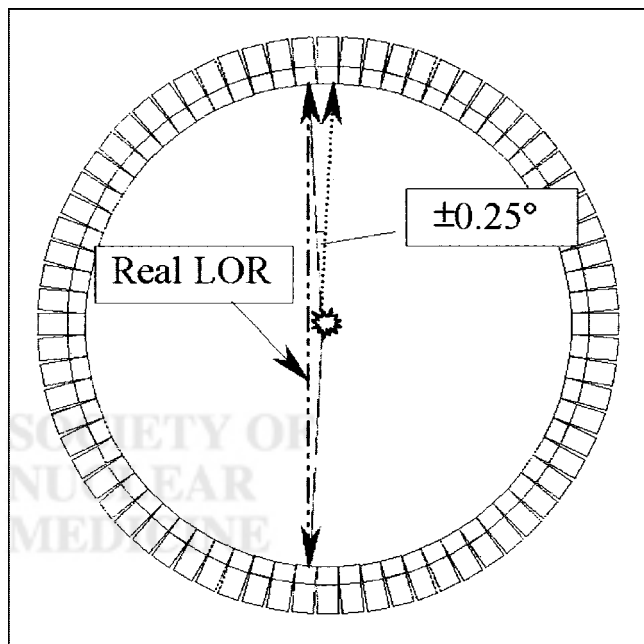


FIGURE 2. Diagram illustrates noncollinearity effect in coincidence imaging.

worsening of the final FWHM value for 80- to 90-cm-diameter PET rings.

Because a necessary condition for positron-electron annihilation is nearly a rest state of both particles, the positron will have to lose its own kinetic energy by interacting with matter. The distance (positron range) covered by the β^+ from the original emission point to the annihilation one depends on its kinetic energy and on the atomic number of crossed tissue. As an example, in water-equivalent matter, positrons emitted by ^{18}F nuclei (maximum energy, 640 keV) have a range of <1 mm, whereas those of ^{82}Rb (maximum energy, 3,350 keV) have a range of about 10 mm. The contribution (R) to the final spatial resolution is assessed as FWHM of the count distribution due to the positron range effect only, resulting in a negligible value of 0.2 mm for ^{18}F and of 2.6 mm for ^{82}Rb (5).

When detection of events is based on block-detector modules and not on scintillation crystals individually coupled to phototubes, a factor (B) should be included to take into account a further degradation of spatial resolution due to mispositioning of events caused by statistical fluctuations in the phototube signals, scatter within the detector, and imperfection in the block-decoding scheme.

When all these effects have been considered, a mathematic estimation of system spatial resolution can then be obtained as (12):

$$FWHM = k_R \cdot \sqrt{C^2 + c^2 + R^2 + B^2}, \quad \text{Eq. 3}$$

where, under the square root, all contributions in quadrature are given as C = noncollinearity effect, c = crystal size, R = positron range, and B = block effect.

k_R is a constant depending on the reconstruction algorithm.

Sensitivity

Sensitivity represents the relationship between the recorded true coincidences and the true activity of a positron-emitting source (10,11,13). The 2 principal elements influencing the sensitivity are the scintillation crystal's efficiency and scanner geometry. The efficiency of the scintillator material is mainly dependent on its density, atomic number, and thickness (the properties of different crystals [Table 1] are described below), whereas the most important geometric component of scanner is the active area of the tomograph seen by annihilation events. As a general consideration, geometric factors for sensitivity depend on the solid angle available for the radioactive source, on its own size dependence, distance, and detector number. Ideally, for perfect geometry, a detector should surround the patient (spheric acquisition system) but, in practice, the most sensitive geometry is the cylindrical one (5,6). A possible formula to compute sensitivity is (9):

$$\text{Sensitivity} = \frac{A \cdot \epsilon^2 \cdot \gamma}{4 \cdot \pi \cdot r^2}, \quad \text{Eq. 4}$$

TABLE 1
Comparison Between Main Physical Properties of PET Scintillation Crystals

Crystal	Relative light output (%)	Decay time (ns)	Density (g·cm ⁻³)	Effective atomic number (Z)	Energy resolution at 511 keV (%)
NaI(Tl)	100	230	3.7	50	8
BGO	15	300	7.1	73	12
LSO	50–80*	40	7.4	65	10
GSO	20–40*	60	6.7	58	9

*Light output depends on cerium concentration and read-out device (PMT or APD).
All crystals emit light with wavelengths ranging from 410 to 480 nm.

where A = detector area seen by each point of the volume to be imaged, ϵ = single detector's efficiency, γ = attenuation factor, and r = detector ring radius.

It is important to consider that sensitivity is proportional to the square of the individual detector efficiency, so that any improvements in crystal efficiency will lead to a 2-fold improvement in final sensitivity. In the next section on 2D or 3D mode, it is explained how the system sensitivity can be improved by increasing the effective detection area by removing any physical interplane shielding (septa).

Noise Equivalent Counting Rate

A useful parameter indicating the noise component of PET data is the noise equivalent counting rate (NECR) (5,6,9,14). The NECR is determined as follows (11):

$$NECR = \frac{T^2}{(T + S + R)}, \quad \text{Eq. 5}$$

where T = trues counting rate, S = scatter counting rate, R = randoms counting rate, and $(T + S + R)$ = prompts or total counting rate.

The NECR represents the ratio between net trues and prompts. The best condition is reached when acquisitions are performed placing an activity concentration in the FOV corresponding to the NECR peak (Fig. 3).

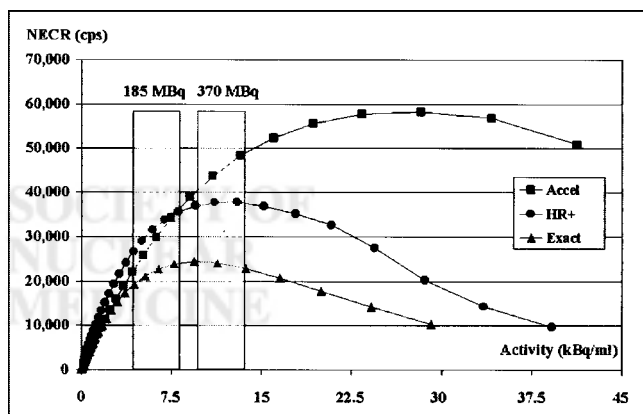


FIGURE 3. NECR profile comparisons between 2 BGO- and LSO-based systems in 3D mode.

Scatter Fraction

In parallel with the NECR, another parameter that is often reported is the scatter fraction (SF). This is defined as follows (10,11):

$$SF = \frac{C_s}{C_{tot}}, \quad \text{Eq. 6}$$

where C_s and C_{tot} are scattered events and total prompt counts, respectively, assessed with a low radioactivity source to assume negligible random events contribution. A narrower acquisition energy window, possible with systems having good energy resolution, will result in a better scatter rejection (Tables 2-4). In Table 3, differences of this parameter are evident, by comparing BGO-based systems (poor energy resolution) with NaI(Tl) or GSO systems, having better energy discrimination capability.

2D OR 3D MODE

Traditionally, PET data acquisitions were based on plane-by-plane LOR detection (2D mode). Direct and cross planes originated from LORs detected within the same ring (difference, 0) or the 2 adjacent rings (ring difference, ± 1), respectively. To shield out-of-plane coincidence photons that are emitted obliquely, annular septa composed of lead-tungsten separate the rings. Commercial state-of-the-art scanners cover an axial FOV of several centimeters; as an example, the ECAT EXACT HR+ (CTI/Siemens, Knoxville, TN) has a 15.5-cm axial FOV and 32 contiguous rings, thereby defining up to 63 contiguous planes (32 direct planes and 31 crossed ones; factory data). In the newer systems, to improve sensitivity, a maximum ring difference of ± 5 can be used without a significant loss of spatial resolution. Working in 2D mode, system sensitivity is constrained, however, to a defined value by geometric acquisition conditions and by electronic collimation fixed between adjacent planes (5–7,9). A large increase in sensitivity can be obtained by collecting all possible LORs by removing the septa. This approach, called 3D acquisition mode (3D mode), produces important changes in the physical performance of the PET scanner that require special 3D reconstruction algorithms. In fact, 2D rebinning techniques ap-

TABLE 2
State-of-the-Art PET Scanners: Technical Features (Factory Data)

Feature	ALLEGRO (Philips- ADAC)	C-PET (Philips- ADAC)	ECAT ART (CTI- Siemens)	ECAT EXACT (CTI- Siemens)	ECAT EXACT HR+ (CTI- Siemens)	ECAT ACCEL (CTI- Siemens)	ADVANCE/ADVANCE Nxi (General Electric)
Number of rings	29	N/A	24	24	32	24	18
Ring diameter (mm)	860	900	824	824	824	824	927
Patient port (mm)	565	560	600	562	562	562	590
Crystals number	17,864	6	4,224	9,216	18,432	9,216	12,096
Crystal material	GSO*	Curved NaI(Tl) [†]	BGO	BGO	BGO	LSO	BGO
Crystal size (mm)	4×6×20	500×300×25.4	6.29×6.29×20	6.29×6.29×20	4.05×4.39×30	6.45×6.45×25	4.0×8.1×30
PMTs number	420	288	264	576	1,152	576	672 (dual)
Crystals/block	No blocks	N/A	64	64	64	64	36
Energy window width (keV)	435–590	435–665	350–650	350–650	350–650	350–650	300–650
Coincidence window (ns)	8	8	12	12	12	6	12.5
Acquisition mode	Full 3D	Full 3D	3D	2D/3D	2D/3D	2D/3D	2D/3D
Transaxial FOV (mm)	576	576 [‡]	600	583	585	585	550
Axial FOV (mm)	180	256	162	162	155	162	152
Number of image planes	90	64/128	47	47	63	47	35
Slice thickness (mm)	2	2	3.375	3.375	2.46	3.375	4.25
Septa material	N/A	N/A	N/A	Lead	Lead	Lead	Tungsten
Septa dimensions (mm)	N/A	N/A	N/A	1×65	0.5×65	1×65	1×117

*PIXELAR.

[†]CCT.

[‡]256 for brain imaging.

N/A = not applicable.

TABLE 3
State-of-the-Art PET Scanners: Physical Performance (Factory Data)

Performance	ALLEGRO (Philips- ADAC)	C-PET (Philips- ADAC)	ECAT ART (CTI- Siemens)	ECAT EXACT (CTI- Siemens)	ECAT EXACT HR+ (CTI- Siemens)	ECAT ACCEL (CTI- Siemens)	ADVANCE/ADVANCE Nxi (General Electric)
Transaxial resolution							
FWHM (mm) at 1 cm					4.6 (2D)	6.2 (2D)	
	4.8*	5.0*	6.2	6.0 (2D/3D)	4.5 (3D)*	6.3 (3D)*	4.8 (2D/3D)
FWHM (mm) at 10 cm					5.4 (2D)	6.7 (2D)	
	5.9*	6.4*	6.9	6.7 (2D/3D)	5.6 (3D)*	7.4 (3D)*	5.4 (2D/3D)
Axial resolution							
FWHM (mm) at 0 cm				4.5 (2D)	4.2 (2D)	4.3 (2D)	4.0 (2D)
	5.4*	5.5*	4.9	4.6 (3D)	4.2 (3D)*	5.8 (3D)*	4.7 (3D)
FWHM (mm) at 10 cm				5.9 (2D)	5.0 (2D)	6.0 (2D)	5.4 (2D)
	6.5*	5.9*	6.6	6.5 (3D)	5.7 (3D)*	7.1 (3D)*	6.3 (3D)
System sensitivity (net trues) (cps/Bq/mL)	19.0*	12.1*	7.3	4.9 (2D) 21.1 (3D)	5.4 (2D) 24.3 (3D)	5.4 (2D) 27.0 (3D)	5.4 (2D) [†] 31.0 (3D) [‡]
Scatter fraction (%)				16 (2D) 36 (3D)	17 (2D) 36 (3D)	16 (2D) 36 (3D)	10 (2D) 35 (3D)

*Assessed according to NEMA NU 2-2001 (11).

[†]Measured at 300-keV LLD in high sensitivity mode.

[‡]Measured at 300-keV LLD.

All parameters were measured following NEMA NU 2-1994 (10) whenever not specified.

TABLE 4
State-of-the-Art PET Scanners: Other Features (Factory Data)

Feature	ALLEGRO (Philips- ADAC)	C-PET (Philips- ADAC)	ECAT ART (CTI- Siemens)	ECAT EXACT (CTI- Siemens)	ECAT EXACT HR+ (CTI- Siemens)	ECAT ACCEL (CTI- Siemens)	ADVANCE/ ADVANCE Nxi (General Electric)
Energy resolution (FWHM)	15%	10%	≈25%	≈25%	≈25%	≈25%	≈25%
Filtered backprojection	Yes (3D)	Yes (3D)	Yes (3D)	Yes (2D/3D)	Yes (2D/3D)	Yes (2D/3D)	Yes (2D/3D)
Iterative algorithms	FORE/OSEM 3D-RAMLA	FORE/OSEM 3D-RAMLA	FORE/OSEM	OSEM (2D) FORE/OSEM	OSEM (2D) FORE/OSEM	OSEM (2D) FORE/OSEM	OSEM (2D)
Transmission source	¹³⁷ Cs	¹³⁷ Cs	¹³⁷ Cs	⁶⁸ Ge	⁶⁸ Ge	⁶⁸ Ge	⁶⁸ Ge
Source activity (MBq)	740 (×1)	185 (×1)	555 (×2)	120 (×3)	140 (×3)	185 (×3)	370 (×2)*
Source geometry	Point source	Point source	Point source	Rod	Rod	Rod	Rod
Transmissive energy window (keV)	600–720	595–860	587–825	350–650	350–650	350–650	300–650
Whole-body scan length (cm)	198	168	195	195	195	195	170

*One additional 55.5-MBq ⁶⁸Ge rod is also installed (for calibration only).

FORE = Fourier rebinning algorithm; OSEM = ordered-subsets expectation maximization algorithm; 3D-RAMLA = 3D row-action maximum-likelihood algorithm.

plied to 3D datasets will result in significant spatial resolution distortion as the radioactivity source moves radially toward the edge of the FOV.

In 3D mode, the sensitivity is approximately 5 times higher than in 2D mode. However, this gain is associated with an increase in random coincidences and scatter fraction, and the increased counting rate can result in loss of events due to dead time (5,6,9,15,16). The scatter fraction may increase from 15%–20% (2D mode) to 30%–40% (3D mode). To overcome the increase in scatter, improvements in energy resolution or institution of mathematic subtraction

methods may be needed (17–19). To fully take advantage of the 3D mode, faster coincidence detection is required, along with higher computing power to manage the very high counting rate. Attempts to overcome these problems have led to a generation of new PET scanners, based on faster electronics and faster scintillation crystals, together with very powerful acquisition or postprocessing techniques (Fig. 4).

PHOTON ATTENUATION

PET images are degraded by photon attenuation due to interactions occurring along the path from the source to the detector (5–9). To detect a coincidence event, the 2 annihilation photons must cross different tissues to reach 2 opposite detectors. If μ is a constant attenuation coefficient along the projection angle and d_1 , d_2 are tissue thickness encountered by two 511-keV photons, the probability of a coincidence detection is given by (5,6,9):

$$P = e^{-\mu \cdot d_1} \cdot e^{-\mu \cdot d_2} = e^{-\mu \cdot (d_1 + d_2)} = e^{-\mu \cdot D}, \quad \text{Eq. 7}$$

showing that attenuation is related to μ and to body thickness (D) along the projection line. When attenuation coefficients along the photon path are not uniform, as is the case for the thorax or abdomen, the contributions from all of the different μ_i -tissues must be considered. The above relation becomes:

$$P = e^{-\sum_{i=0}^x \mu_i \cdot d_{i,1}} \cdot e^{-\sum_{i=x}^l \mu_i \cdot d_{i,2}} = e^{-\sum_{i=0}^l \mu_i \cdot d_i}, \quad \text{Eq. 8}$$

where l is the “ i ” index value corresponding the body thickness D and x is the relative value corresponding to the source location within the body.

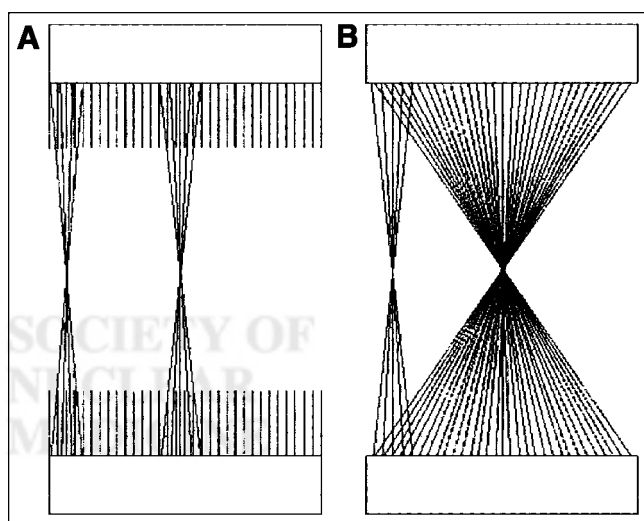


FIGURE 4. Comparison between 2D (A) and 3D (B) acquisition modality. Septa removal causes significant sensitivity improvement when moving radioactive sources toward center of FOV.

Obviously, when photon attenuation increases, P becomes smaller, thus reducing image statistics in all acquired projections.

Therefore, according to Equation 7 for objects with uniform μ , a very simple analytic correction can be made by knowing the thickness (D) along all angular directions. This model can be applied to only a few clinical situations, such as brain imaging, without producing significant inaccuracies of radiotracer quantification.

The majority of PET studies are performed on emitters characterized by a nonuniform attenuation coefficient (NUAC) distribution, making it necessary to implement transmissive acquisitions to estimate NUAC factors. Actually, available scanners use 2 different kinds of transmission sources: (a) ^{68}Ge (β^+ -emitter; transmission data are collected as coincidence events) and (b) ^{137}Cs (γ -emitter of 662 keV; transmission data are collected as single events).

Emitted data correction is performed by following these steps:

1. Mathematic computation of I_0/I (where I_0 is a "blank" scan and I is the acquired transmission scan) obtaining, for each LOR:

$$\frac{I_0}{I} = e^{\sum \mu_i d_i} \quad \text{Eq. 9}$$

2. Algebraic multiplication of each obtained value by the corresponding emissive one.

When using ^{137}Cs , additional steps will be required before point 2: (a) μ -map reconstruction, (b) application of a scaling factor accounting for energy difference (662 vs. 511 keV), and (c) forward projection to obtain the scaled projections set.

Actually, transmissive studies performed using ^{68}Ge sources have very low counting statistics, requiring long scan times to gather enough events to ensure good accuracy of the measurement of attenuation factors. To reduce transmission scan time, particularly important for multibed acquisitions, the accuracy and precision of μ -estimation can be improved by applying the segmentation procedure to low-counting statistics acquisitions. Using this approach, based on knowledge of a priori μ -values, transmission scan times can be reduced from 10–15 min to 1–2 min per bed without significant differences on attenuation values estimation (20–25).

NEW SCINTILLATION CRYSTALS

The physical characteristics of the detector crystal are important for determining the final sensitivity and counting rate capability of a PET imaging system. The ideal scintillator should have fast and intense emission of scintillation light, high atomic number, and high light output.

An important feature of scintillation crystals is energy resolution, which is expressed in terms of FWHM of energy

light output peak and indicates the ability of the detection system to distinguish 2 γ -rays having similar energies. Good energy resolution allows better scatter rejection with consequent improvement of image quality.

Other required features are the mechanical ruggedness of the crystal for easier manufacturing and production and independence from environmental temperature and humidity. It is worth considering that, in spite the high hygroscopicity of NaI(Tl), considered in the past one of the limiting factors to make small crystals, today pixelated detectors of even 1-mm NaI(Tl) pixels (Saint-Gobain Crystals and Detectors, Paris, France) are available. Other important issues are the cost and availability of the scintillation material (5,6,9,26).

In the past few years, a great deal of effort has gone into developing new crystal materials, such as LSO and GSO, to overcome some of the limitations presented by NaI(Tl) and BGO crystals that have been traditionally used for coincidence PET systems (27–31).

As we can see in Table 1, NaI(Tl) is still superior in terms of relative light output and energy resolution to LSO and GSO, whereas these newer materials have faster scintillation emission, which results in significant improvement in tomograph counting-rate capability when coupled to faster acquisition electronics. This concept is represented graphically on Figure 3, where BGO- and LSO-based PET systems are compared in terms of NECR.

By comparing LSO and GSO, LSO has mainly better timing resolution, due to faster decay time, and higher light output than GSO and then better randoms rejection by using a shorter coincidence window (6 ns vs. 8 ns); on the other hand, GSO has better energy resolution, allowing the implementation of narrower energy windows leading to a better scatter rejection.

PET SCANNER GEOMETRY

Improvements in technical performance of the scanner are always associated with higher cost, which becomes a limiting factor for the spread of clinical PET imaging. More than 60% of the cost of a scanner is due to the detection electronics (4). As a result, manufacturers have developed systems with different geometry, permitting scaling of the cost and performance to satisfy the needs of different PET clinical applications.

In this section, the principal technical features and physical performance of PET systems now in use are presented (Tables 2–4). PET systems, based on detector geometry, are classified as full ring, partial ring, and hybrid gamma cameras.

Full Ring

With few exceptions, state-of-the-art dedicated PET scanners are full-ring systems—that is, scintillation detectors cover a full 360° around the volume to be imaged. Advantages offered by this particular configuration are (a) optimal system sensitivity, which is necessary to obtain high count-

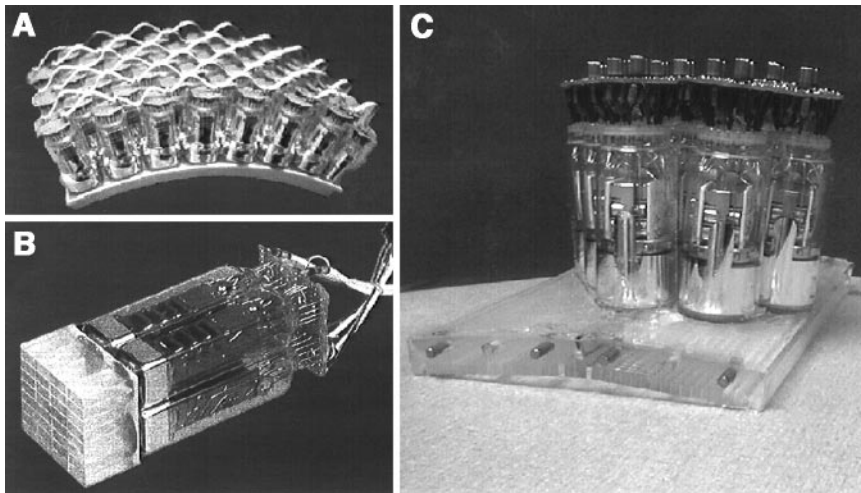


FIGURE 5. Images represent curved crystal (A), block detector (B), and PIXELAR module (C).

ing statistics to achieve the needed physical detector resolution; (b) reduction of image artifacts due to tracer, organ, or patient motion; and (c) absence of moving components (slip ring or rotating heads), which would require further calibrations and would introduce additional variables to be considered.

A further subdivision is based on detection surface structure. In fact, 3 different types of detector modules can differentiate full-ring scanners (9,31–36):

1. Block detector based on 8×8 or 6×6 BGO or LSO crystal blocks coupled to 4 PMTs. In this case, Anger logic allows the localization of the scintillation element belonging to the block where the γ -ray was absorbed. The relative schematic structure is represented below (CTI, Siemens, and General Electric).
2. Curved crystal where the full-ring geometry is obtained by placing side by side 6 curved NaI(Tl) crystals 2.54-cm thick, coupled to 48 PMTs each. A further division of each crystal into subzones is obtained electronically, to increase counting-rate capability (C-PET; Philips-ADAC Medical Systems, Milpitas, CA).
3. PIXELAR module consisting of a curved matrix constituted by 628 (22×29) GSO crystals, fixed onto a continuous light guide. As for the C-PET, the full-ring geometry is realized by placing 28 modules

side by side, coupled to a total of 420 PMTs closely packed in an hexagonal array (ALLEGRO; Philips-ADAC Medical Systems) (Fig. 5).

Partial Ring

Two opposed curved matrices constituted by $33 \times 8 \times 8$ BGO crystal blocks (11 tangentially \times 3 axially) with a reciprocal 15° angular shift rotate, supported by a slip ring technology at 30 rpm. The 2 block banks are not perfectly opposed to increase the transverse FOV during detector rotation (ECAT ART; CTI, Inc., Knoxville, TN) (37,38).

Compared with full-ring systems, this category is characterized by lower overall sensitivity. Using this dedicated scanner, only 3D acquisition is possible. A schematic representation of full-ring and partial-ring gantries using block detector technology is shown in Figure 6.

Hybrid Gamma Cameras

The great clinical usefulness of PET led to the development of double- or triple-head hybrid gamma cameras that are able to perform both PET and SPECT imaging (4–9).

For 511-keV photon detection, the electronics are switched on coincidence modality. Usually dual-head gamma cameras use a 12-ns time window, which is shortened to 10 ns for triple-head systems to slightly reduce the increase in random events that are introduced by the additional detector (factory data).

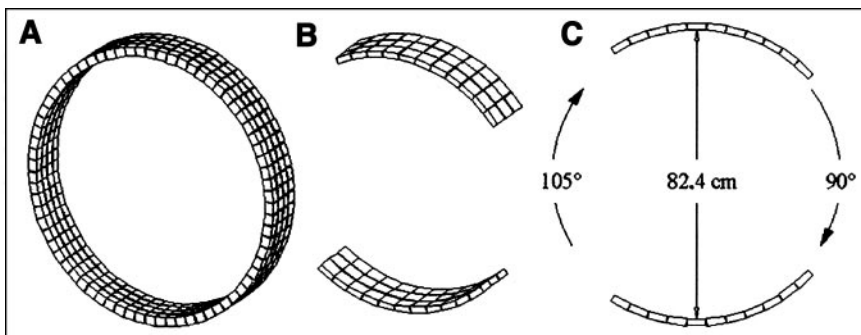


FIGURE 6. Graphic representation of full-ring (A) and partial-ring (B) dedicated PET scanner. (C) Fifteen-degree opposed matrix misalignment is visible.

The main negative aspects of these systems, when used in coincidence mode, are the low sensitivity and the high dead time. The former is strongly affected by head geometry, due to the spaces between the detectors (in a triple-head system, this is partially compensated by the third head), and by the low detection efficiency of NaI. To reach the best compromise between high spatial resolution at low energy (SPECT) and good sensitivity at 511 keV (PET), 1.59- and 1.91-cm NaI(Tl) crystals are used instead of the conventional 0.95-cm ones. With 1.91-cm crystals, sensitivity results in 26% of prompt coincidences with respect to 12% in the case of the 0.95-cm crystal. The significant gamma camera dead time is due to the large coincidence detection area and can be reduced by electronic subdivision into subzones.

The recent introduction of nonuniform attenuation correction has further improved image quality and lesion detectability provided by these systems.

Even if their full clinical applicability for ^{18}F -FDG studies is under examination, hybrid gamma cameras could be used for oncologic patients to evaluate the effectiveness of therapy follow-up (39,40).

WHOLE-BODY IMAGING

Having considered the technical features and physical performance of dedicated PET, we can better understand the requirements for oncologic whole-body PET imaging: short scan times, good lesion detectability, and accurate radiotracer quantification.

Until recently, one of the main limitations of PET that prevented practical whole-body imaging was the short axial FOV of the scanner. Without an adequate axial detector length and a moving whole-body scanning bed, acquisition of sufficient numbers of counts along an acceptable axial length required excessively long scan times, making clinical application very difficult (1–7).

With the introduction of new PET instrumentation with a 15- to 25-cm axial FOV and, subsequently, the ability to perform 3D acquisition, the sensitivity of the scanner has been markedly increased (4–6,9,15–19). Optimal 3D acquisition

requires fast scintillation crystals and the electronics needed for good timing and energy resolution to reduce dead time, randoms events, and the scatter fraction (9,15–19). The newest GSO- and LSO-based scanners, working without interplane septa, permit acceptance of higher activities in the FOV. With their fast scintillation time and coincidence electronics, these crystals can acquire at high coincidence counting rates with good signal-to-noise ratio, thereby performing attenuation-corrected whole-body studies within 30 min or less (factory data).

Whole-body imaging is performed by acquiring multiple contiguous body views by moving the bed through the tomograph, up to 200-cm maximum length. Once the acquisition time for each bed position has been determined, the total scan time depends on the patient height and the effective axial FOV of the scanner per bed position. The effective axial FOV is less than the real FOV because planes near the edge, where sensitivity decreases, are overlapped to avoid image artifacts due to poor counting statistics. As a result, it is necessary to overlap adjacent bed positions in whole-body studies. An even larger overlap between adjacent positions (up to 35%–50% of axial FOV) is needed in acquiring data in 3D mode with septa removed (16). The 4- to 5-fold increase in system sensitivity that results from all events within the FOV being seen by the scanner produces a sensitivity profile with a maximum in the center of the FOV, with rapid decrease on moving away from the peak. Primarily for this reason, multibed acquisitions for whole-body studies need to reduce the axial FOV to maintain a uniform counting profile. This results in an increase of the number of beds needed to cover the same patient length (Fig. 7), thereby increasing total acquisition time. For some systems (C-PET or ALLEGRO), large bed overlaps seem dictated also by transmission scan axial FOV (36).

Another important parameter that strongly affects total scan time is the acquisition of the attenuation-correction scan. Depending on source type and strength, the time required to collect a sufficient number of counts will vary. In particular, there is a major difference between ^{68}Ge and

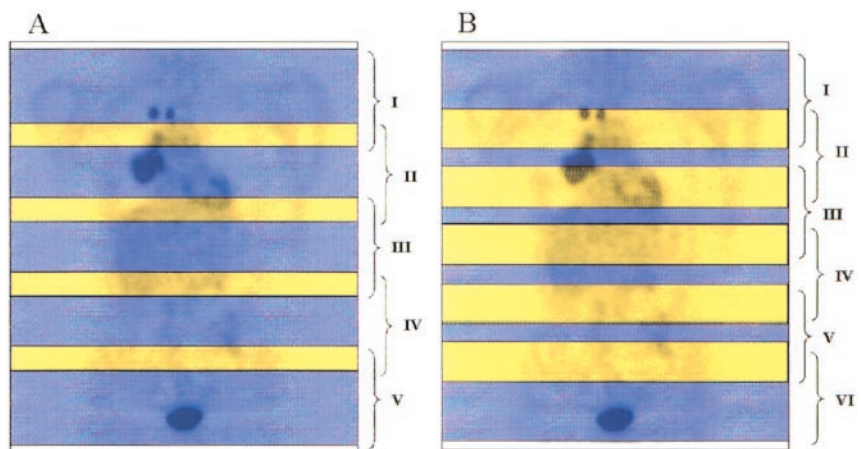


FIGURE 7. Comparison of 2D (A) and 3D (B) bed overlap whole-body studies. With same axial FOV, increased 3D overlap requires (as example) additional bed length to cover same axial length.

^{137}Cs transmission sources. Considering equal source activity, ^{68}Ge is characterized by much lower counting rates than ^{137}Cs , because acquisition in coincidence mode results in rejection of $>95\%$ of emitted singles, as well dead-time problems in the detectors closer to the rod source, thereby limiting the usable rod activity (22–24,37,38).

Acquisition of coincidence transmission scans with source windowing allows acquisition after injection because it results in reduction of emission contamination, which could otherwise lead to underestimation of μ -map values (22). A further reduction in transmission acquisition time is achieved by the use of segmentation in attenuation correction. This allows reduction of the required time to 1–2 min per bed without losing μ -map accuracy or precision (20,21).

On the other hand, with a ^{137}Cs collimated point source (555–740 MBq), transmission images can be acquired on scanners having energy resolution to discriminate 511-keV (patient emission) from 662-keV (^{137}Cs γ -ray energy) photons.

PET/CT INSTRUMENTATION

The ability of ^{18}F -FDG PET to detect tumors by changes in glucose metabolism has had a major impact on the diagnosis, staging, and follow-up of oncologic patients. In early stages of tumor growth, metabolic alterations may be detected before anatomic changes are apparent. The disadvantage of functional PET imaging is its relatively low resolution of ≈ 4.0 - to 4.5-mm FWHM at best, leading to lack of anatomic information. There is little relative difference in ^{18}F -FDG uptake between most normal tissues so that one often cannot separate adjacent tissues (e.g., bone and muscle) in PET images. Because of this, anatomic localization of lesions is frequently limited. As a result, great efforts have been made to obtain registration of PET and CT images to add the anatomic accuracy of CT to the metabolic accuracy of PET (41–45).

When attempts are made to fuse PET and CT images, several problems are encountered (41–49): (a) The 2 studies (PET and CT) are performed on different scanners, and bed profiles (and, consequently, organ positions) can be significantly different; (b) because PET acquisition is often performed several days after the CT scan, repositioning may not be accurate and internal organs shifts can take place; (c) during CT, patients keep their arms over the head (to reduce attenuation and beam hardening effects), but because PET acquisition requires approximately 40 min, this is often not feasible; and (d) to reduce movements artifacts, CT is acquired in breath-holding conditions, though for obvious reasons this cannot be done in 35- to 40-min-long PET acquisitions. All of these factors can result in major changes in body profiles and variations in organ position, thus making the fusion of PET and CT images very difficult, even when innovative registration programs or elastic 3D models for chest image transformation are used.

A good solution to the above points is the acquisition of both studies on the same scanner, essentially at the same

time, combining the PET and CT components in a single gantry. CT and PET studies are acquired sequentially during the same scan, ensuring same bed profile, no repositioning, and very little time between the 2 acquisitions.

However, some difficulties still remain: (a) The CT acquisition should be performed without usual breath-holding and with arms down when PET is not feasible with arms over the head, to optimize image fusion; and (b) the CT scan should be performed without injecting contrast agent to avoid noncorrectable changes in attenuation map used for 511-keV photons.

These points must be considered because CT is also used to correct attenuation of emissive PET images (46–49). The proposed protocol (46) consists of a first segmentation of the CT images, to separate soft tissue and bone, followed by the application of 2 different scaling factors to obtain a 511-keV-equivalent μ -map.

Considering the first point, the main problem is that the limited CT FOV leads to arm truncation and a subsequent underestimation of attenuation correction factor (ACF), because μ -values outside the CT FOV are set to 0. A possible solution is to estimate μ -values in truncated projections, resulting in a reduction of CT ring artifacts and a great recovery in PET-corrected images (47).

It is worth considering that the use of contrast agent, which is necessary in oncologic imaging, can affect attenuation-corrected PET images at different levels of inaccuracy (47). When transmissive scans are acquired with ^{68}Ge or ^{137}Cs sources, μ -maps show differences of about 2% between regions of high and low contrast agent concentration. If the CT scan is used to estimate 511-keV μ -maps, during the segmentation phase, contrast agent can be easily confused with bone tissue because of the high Z value, resulting in overestimation of PET ACFs and, consequently, radiotracer concentration by about 10%. A possible correction could involve morphologic segmentation, where bone and contrast agent contributions would be manually selected, to be evaluated separately.

Finally, breath-holding conditions are permanent obstacles to good image coregistration and correct μ -map estimation. One possible solution is to allow respiration during the CT scan, thus reducing errors in μ -maps, but reducing the quality of anatomic information near the anterior chest wall. Some authors (48) have established that the best solution to the problem is the “normal-expiration and breath-hold” protocol. The worst results were obtained using the “maximum-expiration and breath-hold” or “maximum-inspiration and breath-hold” protocol because of the great differences between PET and CT section profiles. In most cases, free breathing was an acceptable solution (Table 5).

2D RECONSTRUCTION ALGORITHMS

Two-dimensional PET image reconstruction estimates the volume radiotracer distribution starting from plane-by-

TABLE 5
 PET/CT Scanners: Main Technical Parameters Relative to CT Scanners Used (Factory Data)

Parameter	Philips GEMINI	CTI REVEAL/CPS BIOGRAPH	General Electric DISCOVERY LS
PET scanner	ALLEGRO	ECAT EXACT HR+ or ECAT ACCEL	ADVANCE Nxi
CT scanner	MX 8000 DUAL	SOMATOM EMOTION DUO	LIGHTSPEED PLUS
Maximum power (kW)	60	40	60
Maximum tube voltage (kV)	140	130	140
Maximum tube current (mA)	500	240	440
Selectable kV values	90, 120, 140	80, 100, 130	80, 100, 120, 140
mA range	30–500	30–240	10–440
Heat capacity (MHU)	6.5	3.5	6.3
Slices/rotation	2	2	4
Slice number × thickness (mm)	2 × 0.5 2 × 1 2 × 2.5 2 × 5 2 × 8 2 × 10	2 × 1 2 × 1.5 2 × 2.5 2 × 4 2 × 5	2 × 0.625 (axial only) 1 and 4 × 1.25 4 × 2.5 4 × 3.75 4 × 5 2 × 7.5 2 × 10
Pitch minimum	0.375	0.25	0.75
Pitch maximum	2	2	1.5
Angular speed (s/rotation)	0.5, 0.75, 1, 1.5, 2	0.8, 1, 1.5	0.5, 0.6, 0.7, 0.8, 0.9, 1, 2, 3, 4
Maximum scan time (s)	60	100	120
Detectors array	672 × 2 (1,344 elements)	672 × 2 (1,344 elements)	912 × 16 (14,592 elements)
Transverse FOV (mm)	500	500	500

MHU = Mega Heat Units.

plane LOR acquisition data by stacking sequentially reconstructed planes. Accordingly, data acquisition consists of uniform angular sampling around the patient. For each considered angle, individual projection elements (or bin) represent the line integral of emitted LORs. For each plane, projection data are stored in a sinogram matrix whose rows and columns represent angular and radial samplings, respectively (15,16,50).

Filtered Backprojection

The first reconstruction algorithm to be used was filtered backprojection. This method provides accurate estimation of 2D radiotracer distribution when projection data are noise free. The basic principles are to perform the Fourier transform of angular projections, apply the ramp filter in the frequency domain, uniformly distribute the filtered data over the reconstructed matrix, and then antitransform (5,15,16,50). This method is simple to implement and fast in performing sections reconstruction. However, the ramp filter used to eliminate the star artifact and improve spatial resolution also amplifies the noise component, which is particularly important at low counting statistics. To compensate for these effects, low-pass smoothing filters are applied to cutoff frequencies higher than a certain limit, thereby producing more blurred images and worsening spatial resolution.

Iterative Algorithms

Iterative algorithms are based on the attempt to maximize or minimize a target function determined by the particular algorithm used. The target is reached through several analytic processes called iterations. A major advantage of this type of algorithm is the possibility of incorporating different a priori information, such as noise component, attenuation, or characteristics of detector nonuniformity, for more accurate image reconstruction; however, it must be pointed out that inclusion of additional parameters means increase in processing times.

Depending on the method, different numbers of iterations are required to reach the target function, keeping in mind that too many iterations can easily lead to noise amplification with image quality deterioration. For this reason, it is important to perform an accurate evaluation of the number of iterations needed to obtain the best image quality (16,50). Different iterative algorithms are present in literature, some based on the methodologies of numeric linear algebra and others based on statistical approaches. To the latter class belongs the maximum-likelihood expectation maximization (MLEM), which is able to estimate more accurate radiotracer distribution. The MLEM is based on the maximization of the logarithm of a Poisson-likelihood target function (16,50–52). The attempt is to obtain a reconstructed slice whose forward projection generates a projection dataset

almost equal to the original one. The main feature of this reconstruction algorithm is to update the image during each iteration by using a multiplicative factor assessed as the ratio between the original acquired projections and the newly estimated ones. Advantages of this iterative method are very low noise amplification without loss of spatial resolution and the fact that all reconstructed values will be positive because a nonnegativity condition is imposed on the original data (16,50–52). The main disadvantage is the large number of iterations required to converge to an optimal solution and then the long processing times, hampering its applicability in clinical routine.

To overcome the problem of slow convergence rate, the ordered-subsets expectation maximization (OSEM) algorithm was proposed in 1994, which is now the most widely used iterative reconstruction method in whole-body PET imaging (53).

The OSEM is a modified version of MLEM (the target is still the maximization of the log-likelihood function) with the main difference being that projections are grouped into subsets having projections uniformly distributed around the volume to be imaged. Within each iteration the target function is updated as many times as the number of subsets, proportionally accelerating convergence. An optimization of subsets and iterations number is required when the method is applied to real, noisy data, because the algorithm can cycle without converging to the MLEM function (53–56). More recently has been proposed the row-action maximum-likelihood algorithm (RAMLA), which in some extension can be considered a special case of OSEM requiring sequences of orthogonal projections and a relaxation parameter to control updating of the log-likelihood objective at each full iteration cycle (57). Theoretically, these 2 conditions should guarantee a faster and better convergence to MLEM solution than OSEM.

3D RECONSTRUCTION ALGORITHMS

A different approach must be followed when treating 3D projection data, because each LOR's axial angle must be taken into consideration together with limitations imposed by scanner geometry (15,16,58). There is a huge volume of data to manage. As an example, in a multiring system having N detector rings, a full 3D acquisition would generate N direct (perpendicular to the scanner axis) and $N(N - 1)$ oblique sinograms (N^2 in total), instead of $2N - 1$, as in the 2D case (16). It is evident that the implementation of such algorithms requires large memory space and complex computation that would result in unacceptable processing time using the workstations available at present for clinical applications.

Dealing with the 3D analytic method, difficulties of its implementation are mainly due to the incomplete sampling of 3D volumes, related to the finite axial extent of the scanner. Unsourced data must be recovered through a first volume estimation obtained with 2D reconstruction of direct

sinograms. Estimated and measured projection data are then reconstructed with 3D filtered backprojection. The 3D filtered backprojection algorithm initially used has been now substituted by new solutions performed in attempts to produce efficient and practical 3D methods for clinical PET systems (50,59–61).

A description of the most commonly used methods implemented on dedicated state-of-the-art high-end scanners now commercially available follows in the next section.

3D Data Rebinning

A rebinning algorithm is a mathematic procedure for rearrangement of 3D data into a set of 2D-equivalent projections (59).

The simplest solution to this problem, which is still implemented on some scanners and hybrid gamma cameras, is offered by the single-slice rebinning algorithm. This consists of assigning axially tilted LORs to transaxial planes intersecting them in their axial midpoints. This approach is reasonably good if applied to small sources placed close to the scanner axis such as the brain. Rough approximations can result when sources move off axis, as is the case in whole-body imaging with more superficial structures.

The Fourier rebinning algorithm is based on the frequency–distance relation for oblique sinograms, in Fourier domain. This rebinning method allows a more accurate estimate of the source axial location, thereby strongly reducing off-axis distortion. After rebinning is performed, all 2D reconstruction algorithms can be used.

3D-RAMLA Reconstruction

The development of fully 3D-dedicated PET scanners required improvement in image quality, through both instrumentation developments as previously described and

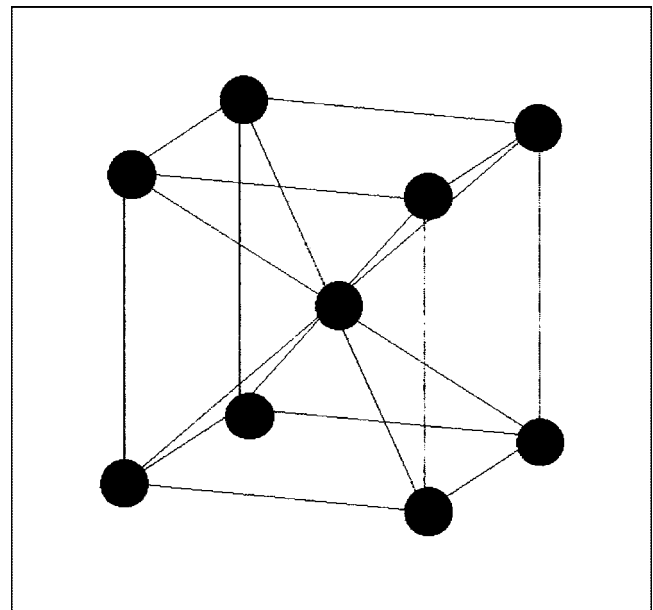


FIGURE 8. Blobs distribution (represented as spheric elements) used for new-conception reconstruction algorithms.

new conception of fully 3D reconstruction algorithms (57,60–65). Nevertheless, even though these algorithms can theoretically achieve good results, they can be problematic in actual implementation because of the heavy computational burden, even with the very powerful processing workstations actually available.

Among fully 3D reconstruction methods proposed by academics, the 3D-RAMLA is currently implemented on some commercial systems and used in clinical practice (C-PET and ALLEGRO). This algorithm has been developed using a new-conception approach based on the substitution of voxels with spherically symmetric volume elements, called blobs, placed on a uniform 3D grid, as shown in Figure 8 (62–65). The great advantage of blobs resides in the possibility of controlling the reconstructed image quality through a priori definition of their amplitude and shape (63,64). To obtain almost-uniform volume sampling, blobs are partially overlapped with neighboring ones and counts in common regions are averaged using weighting schemes. Implementation of the 3D-RAMLA + blob on a fully 3D PET system demonstrated good performance (65) on yielding high-quality images even though up to 25 min are actually necessary to reconstruct the image volume (factory data).

CONCLUSION

The use of ^{18}F -FDG PET imaging is rapidly increasing along with the number and variety of coincidence detection systems. An overview of different PET scanners commercially available has been presented by reporting physical and technical performance and analyzing specific features available for whole-body imaging. To allow a better understanding of the main differences among the considered systems, some basic principles of coincidence detection and physical effects affecting PET images were also mentioned.

By comparing different scanners, full-ring systems should be preferred for the higher sensitivity to partial-ring or coincidence cameras, despite the higher cost, to take full advantage of potential spatial resolution, fundamental request for oncologic studies, and to speed up the patient throughput in those departments with high clinical workload. The new faster LSO and GSO systems, because of their improved counting-rate capability, seem promising for full 3D PET applications. However, high-performance 3D reconstruction algorithms and scatter correction procedures along with powerful workstations are required to transfer these systems into clinical routine.

PET/CT has been included as a new instrument capable of improving ^{18}F -FDG PET diagnostic accuracy for oncologic patients by supplying high-resolution anatomic references to correspondent lower resolution metabolic images of body tissues.

The new PET scanners present good potentiality on improving accuracy and image quality of ^{18}F -FDG PET whole-body studies; nevertheless, new developments are

still a work in progress to optimize acquisition procedures and reconstruction algorithms.

ACKNOWLEDGMENTS

The authors are grateful to Dr. Peter Valk for his helpful suggestions. Thanks are also due to Philips Medical Systems, General Electric Medical Systems, CTI/Siemens, and OMNIA for their interest on supplying factory data.

REFERENCES

1. Coleman RE, Ruth RD. A perspective on clinical PET imaging. *Clin Positron Imaging*. 1999;2:297–299.
2. Nutt R. The history of positron emission tomography. *Mol Imaging Biol*. 2002; 4:11–26.
3. Rich DA. A brief history of positron emission tomography. *J Nucl Med Technol*. 1997;25:4–11.
4. Phelps ME, Cherry SR. The changing design of positron imaging systems. *Clin Positron Imaging*. 1998;1:31–45.
5. Cherry SR, Phelps ME. Positron emission tomography: methods and instrumentation. In: Sandler MP, Coleman RE, Wackers FJT, Patton JA, Gottschalk A, Hoffer PB, eds. *Diagnostic Nuclear Medicine*. 3rd ed. Baltimore, MD: Williams & Wilkins; 1996:139–159.
6. Hoffman EJ, Phelps ME. Positron emission tomography: principles and quantification. In: Phelps ME, Mazziotta JC, Schelbert RH, eds. *Positron Emission Tomography and Autoradiography: Principles and Applications for the Brain and Heart*. New York, NY: Raven Press; 1986:237–286.
7. Turkington TG. Introduction to PET instrumentation. *J Nucl Med Technol*. 2001;29:1–8.
8. Daghighian F, Sumida R, Phelps ME. PET imaging: an overview and instrumentation. *J Nucl Med Technol*. 1990;18:5–13.
9. Budinger TF. PET instrumentation: what are the limits? *Semin Nucl Med*. 1998;28:247–267.
10. National Electrical Manufacturers Association. *NEMA Standards Publication NU 2-1994: Performance Measurements of Positron Emission Tomographs*. Washington, DC: National Electrical Manufacturers Association; 1994.
11. National Electrical Manufacturers Association. *NEMA Standards Publication NU 2-2001: Performance Measurements of Positron Emission Tomographs*. Rosslyn, VA: National Electrical Manufacturers Association; 2001.
12. Moses WW, Derenzo SE. Empirical observation of resolution degradation in positron emission tomographs utilizing block detectors [abstract]. *J Nucl Med*. 1993;34(suppl):101P.
13. Bailey DL, Jones T, Spinks TJ. A method for measuring the absolute sensitivity of positron emission tomographic scanners. *Eur J Nucl Med*. 1991;18:374–379.
14. Strother SC, Casey ME, Hoffman EJ. Measuring PET scanner sensitivity: relating count rates to image signal-to-noise ratios using noise equivalent counts. *IEEE Trans Nucl Sci*. 1990;37:783–788.
15. Badawi RD. *Aspects of Optimization and Quantification in Three-Dimensional Positron Emission Tomography* [PhD thesis]. London, U.K.: University of London; 1998:20–159.
16. Bendriem B, Townsend DW. *The Theory and Practice of 3D PET*. Dordrecht, The Netherlands: Kluwer Academic; 1998.
17. Watson CC, Newport D, Casey ME. A single scatter simulation technique for scatter correction in 3D PET. In: Grangeat P, Amans JL, eds. *Three-Dimensional Image Reconstruction in Radiology and Nuclear Medicine*. Dordrecht, The Netherlands: Kluwer Academic; 1996:255–268.
18. Zaidi H. Comparative evaluation of scatter correction techniques in 3D positron emission tomography. *Eur J Nucl Med*. 2000;27:1813–1826.
19. Brasse D, Kinahan PE, Lartizen C, et al. Correction methods for random coincidences in 3D whole body PET imaging. *IEEE Nucl Sci Symp Med Imaging Conf Rec*. 2001;4:2080–2084.
20. Xu EZ, Mullan NA, Gould KL, Anderson WL. A segmented attenuation correction for PET. *J Nucl Med*. 1991;32:161–165.
21. Bettinardi V, Pagani E, Gilardi MC, et al. An automatic classification technique for attenuation correction in positron emission tomography. *Eur J Nucl Med*. 1999;26:447–458.
22. Jones WF, Digby WM, Luk WK. Optimizing rod window width in positron emission tomography. *IEEE Trans Med Imaging*. 1995;14:266–270.
23. Watson CC, Jones WF, Brun T, Baker K, Vaigneur K, Young J. Design and performance of a single photon transmission measurement for the ECAT ART. *IEEE Nucl Sci Symp Med Imaging Conf Rec*. 1997;2:1366–1370.

24. Jones W, Vaigneur K, Young J, Reed J, Mojers C, Nahmias C. The architectural impact of single photon transmission measurements on full-ring 3-D positron tomography. *IEEE Nucl Sci Symp Med Imaging Conf Rec.* 1995;2:1026–1030.
25. Meikle SR, Bailey DL, Hooper PK, et al. Simultaneous emission and transmission measurements for attenuation correction in whole-body PET. *J Nucl Med.* 1995;36:1680–1688.
26. Melcher CL. Scintillation crystals for PET. *J Nucl Med.* 2000;41:1051–1055.
27. Muehllehner G, Hümmich Y. Sodium iodide positron detectors: PET/SPECT and dedicated systems. *Revue de l'ACOMEN.* 1999;5:145–151.
28. Saoudi A, Pepin C, Pépin C, Houde D, Lecomte R. Scintillation light emission studies of LSO scintillators. *IEEE Trans Nucl Sci.* 1999;46:1925–1928.
29. Knoess C, Gremillion T, Schmand M, et al. Development of a daily quality check procedure for the high resolution research tomograph (HRRT) using natural LSO background radioactivity. *IEEE Nucl Sci Symp Med Imaging Conf Rec.* 2001;2:1115–1119.
30. Nutt R, Melcher CL. Current and future development with LSO: a scintillator with excellent characteristics for PET. *Revue de l'ACOMEN.* 1999;5:152–155.
31. Surti S, Karp JS, Freifelder R, Liu F. Optimizing the performance of a PET detector using discrete GSO crystals on a continuous lightguide. *IEEE Trans Nucl Sci.* 2000;47:1030–1036.
32. Brix G, Zaers J, Adam LE, et al. Performance evaluation of a whole-body PET scanner using the NEMA protocol. *J Nucl Med.* 1997;38:1614–1623.
33. Eriksson L, Wienhard K, Eriksson M, et al. NEMA evaluation of the first and second generation of the ECAT EXACT HR family of scanners. *IEEE Nucl Sci Symp Med Imaging Conf Rec.* 2001;3:1223–1226.
34. DeGrado TR, Turkington TG, Williams JJ, Stearns CW, Hoffman JM, Coleman RE. Performance characteristics of a whole-body PET scanner. *J Nucl Med.* 1994;35:1398–1406.
35. Lewellen TK, Kohlmyer SG, Miyaoka RS, Kaplan MS, Stearns CW, Schubert SF. Investigation of the performance of the General Electric Advance positron emission tomograph in 3D mode. *IEEE Trans Nucl Sci.* 1996;43:2199–2207.
36. Adam LE, Karp JS, Daube-Whitherspoon ME, Smith RJ. Performance of a whole-body PET scanner using curve-plate NaI(Tl) detectors. *J Nucl Med.* 2001;42:1821–1830.
37. Townsend DW, Wensveen M, Byars LG, et al. A rotating PET scanner using BGO block detectors: design, performance and applications. *J Nucl Med.* 1993;34:1367–1376.
38. Bailey DL, Young H, Bloomfield PM, et al. ECAT ART: a continuously rotating PET camera—performance characteristics, initial clinical studies and installation considerations in a nuclear medicine department. *Eur J Nucl Med.* 1997;24:6–15.
39. Landoni C, Gianolli L, Lucignani G, et al. Comparison of dual-head coincidence PET versus ring PET in tumor patients. *J Nucl Med.* 1999;40:1617–1622.
40. Ak I, Blokland JAK, Pauwels EKJ, Stokkel MPM. The clinical value of ¹⁸F-FDG detection with a dual-head gamma camera: a review. *Eur J Nucl Med.* 2001;28:763–778.
41. Townsend DW, Beyer T, Kinahan PE, et al. The SMART scanner: a combined PET/CT tomograph for clinical oncology. *IEEE Nucl Sci Symp Med Imaging Conf Rec.* 1998;2:1170–1174.
42. Beyer T, Townsend DW, Brun T, et al. A combined PET/CT scanner for clinical oncology. *J Nucl Med.* 2000;41:1369–1379.
43. Beyer T, Watson CC, Meltzer CC, Townsend DW, Nutt R. The Biograph: a premium dual modality PET/CT tomograph for clinical oncology. *Electromedica.* 2001;2:120–126.
44. Townsend DW, Beyer T, Kinahan PE, et al. Fusion imaging for whole-body oncology with a combined PET and CT scanner [abstract]. *J Nucl Med.* 1999;40(suppl):148P.
45. Charron M, Beyer T, Kinahan PE, Meltzer CC, Dachille MAA, Townsend DW. Whole-body FDG PET and CT imaging of malignancies using a combined PET/CT scanner [abstract]. *J Nucl Med.* 1999;40(suppl):256P.
46. Kinahan PE, Townsend DW, Beyer T, Sashin D. Attenuation correction for a combined 3D PET/CT scanner. *Med Phys.* 1998;25:2046–2053.
47. Carney J, Beyer T, Yap JT, Townsend DW. CT-based attenuation correction for PET/CT scanners. *IEEE Nucl Sci Symp Med Imaging Conf Rec.* 2001 [on CD-ROM].
48. Goerres GW, Kamel E, Heidelberg TNH, Schwitler MR, Burger C, von Schulthess GK. PET-CT image co-registration in the thorax: influence of respiration. *Eur J Nucl Med.* 2002;29:351–360.
49. Kamel E, Hany TF, Burger C, et al. CT vs ⁶⁸Ge attenuation correction in a combined PET/CT system: evaluation of the effect of lowering the CT tube current. *Eur J Nucl Med.* 2002;29:346–350.
50. Townsend DW, Defrise M. Image reconstruction methods in positron tomography. *CERN (European Organization for Nuclear Research) Report 93-0.2.* Geneva, Switzerland; 1993.
51. Miller TR, Wallis JW. Fast maximum-likelihood reconstruction. *J Nucl Med.* 1992;33:1710–1711.
52. Miller TR, Wallis JW. Clinically important characteristics of maximum-likelihood reconstruction. *J Nucl Med.* 1992;33:1678–1684.
53. Hudson HM, Larkin RS. Accelerated image reconstruction using ordered subsets of projection data. *IEEE Trans Med Imaging.* 1994;13:601–609.
54. Riddell C, Carson RE, Carrasquillo JA, et al. Noise reduction in oncology FDG PET images by iterative reconstruction: a quantitative assessment. *J Nucl Med.* 2001;42:1316–1323.
55. Boellaard R, Van Lingen A, Lammertsma AA. Experimental and clinical evaluation of iterative reconstruction (OSEM) in dynamic PET: quantitative characteristics and effects on kinetic modeling. *J Nucl Med.* 2001;42:808–817.
56. Lonnew M. Attenuation correction in whole-body FDG oncological studies: the role of statistical reconstruction. *Eur J Nucl Med.* 1999;26:591–598.
57. Browne J, De Pierro AR. A row-action alternative to the EM algorithm for maximizing likelihoods in emission tomography. *IEEE Trans Med Imaging.* 1996;15:687–699.
58. Daube-Whitherspoon ME, Muehllehner G. Treatment of axial data in three-dimensional PET. *J Nucl Med.* 1987;28:1717–1724.
59. Defrise M, Kinahan PE, Townsend DW, Michel C, Sibomana M, Newport DF. Exact and approximate rebinning algorithms for 3-D PET data. *IEEE Trans Med Imaging.* 1997;16:145–158.
60. Liow JS, Strother SC, Rehm K, Rottenberg DA. Improved resolution for PET volume imaging through three-dimensional iterative reconstruction. *J Nucl Med.* 1997;38:1623–1631.
61. Kinahan PE, Rogers JG. Analytic 3D image reconstruction using all detected events. *IEEE Trans Nucl Sci.* 1989;36:964–968.
62. Matej S, Lewitt RM. Efficient 3D grids for image reconstruction using spherically-symmetric volume elements. *IEEE Trans Nucl Sci.* 1996;42:1361–1370.
63. Matej S, Lewitt RM. Practical considerations for 3-D image reconstruction using spherically symmetric volume elements. *IEEE Trans Med Imaging.* 1996;15:68–78.
64. Jacobs F, Lemahieu I. Iterative image reconstruction from projections based on generalised Kaiser-Bessel window functions. In: *Proceedings of the 1st World Congress on Industrial Tomography 1999.* Buxton, U.K. April 14–17, 1999:427–432. Available at: http://www.vcipt.org.uk/congress/profiles/s2_3.pdf. Accessed April 3, 2003.
65. Daube-Whitherspoon ME, Matej S, Karp JS, Lewitt RM. Application of the 3D row action maximum likelihood algorithm to clinical PET imaging. *IEEE Trans Nucl Sci.* 2001;48:24–30.

